AIAA AVIATION Forum
June 15-19, 2020, VIRTUAL EVENT
AIAA AVIATION 2020 FORUM

10.2514/6.2020-2943

Numerical Investigation of Wingtip Vortices of Coflow Jet Active Flow Control Wings

Jeremy Boling*, Ge-Cheng Zha†
Department of Mechanical and Aerospace Engineering
University of Miami, Coral Gables, Florida 33124
E-mail: gzha@miami.edu

Aaron Altman‡
Aerodynamic Technology Branch,
Aerospace Systems Directorate, AFRL/RQVA
Wright-Patterson AFB, Ohio 45433

This paper investigates the wingtip vortices and their feeding shear-layer interactions for a 3D Co-Flow Jet (CFJ) wing and a baseline wing at cruise conditions at an aspect ratio of 10. The wings are based on a NACA 6421 airfoil, with the CFJ airfoil containing injection and suction slots for active flow control. A momentum coefficient C_μ of 0.03 is used at the cruise condition at $\alpha = 5^\circ$ based on the optimum aerodynamic efficiency found in a previous study. The total pressure of the injection slot is fixed at this value for the entire angle of attack sweep from $\alpha = -1^\circ$ to $\alpha = 26^\circ$. The simulations employ the validated in house FASIP CFD code, utilizing a 3D RANS solver with Spalart-Allmaras (S-A) turbulence model, 3rd order WENO scheme for the inviscid fluxes, and 2nd order central differencing for the viscous terms. The maximum aerodynamic efficiency occurs at an AoA of 2°, across which the vortex core axial velocity remains mostly wake-like in the near wake region. However, the axial velocity in the vortex core edge increases with jet-like axial velocity when the AoA is at 5°. At the high AoA of 12°, the core axial velocity has a strong jet in the near wake region. With the tip vortex growing in size while propagating downstream, an adverse pressure gradient is created as predicted by Batchelor's model. At this point the axial velocity decreases to a wake-like profile. This phenomenon is observed for both the CFJ and baseline wings. The CFJ wing expectedly produces more lift than its baseline counterparts at the same angle of attack. This results in a smaller wake-momentum deficit at lower angles of attack, and a stronger jet-like axial velocity profile at higher angles of attack. The vortex core axial velocity profile and vortex tangential velocity profiles are linked. When greater axial velocity is observed in the core region, higher the tangential velocity is also observed. The overall strength of the tip vortex is greater for the CFJ wing, compared to the baseline wing at the same angle of attack. The free-shear layer roll-up is also examined and indicates a corresponding increase in absolute magnitude for the CFJ when compared to the baseline wing.

Nomenclature

V	Flow Velocity
ρ	Air Density
α, AoA	Angle of Attack
$\dot{m}$	Mass Flow Rate
M	Mach Number

*Graduate Research Assistant
†Professor, AIAA Associate Fellow
‡Tech Advisor, AIAA Associate Fellow

M_i	Isentropic Mach Number
Re	Reynolds Number
L	Aerodynamics Lift
D	Aerodynamic Drag
u	x-Component Velocity in Cartesian Coordinates
v	y-Component Velocity in Cartesian Coordinates
w	z-Component Velocity in Cartesian Coordinates
V_t	Azimuthal (Tangential) Velocity Describing the Tip Vortex
p	Static Pressure
p_0	Total Pressure
η	Pumping Power
q_∞	Freestream Dynamic Head, $\frac{1}{2}\rho_\infty {V_\infty}^2$
C_L	Lift Coefficient, $\frac{L}{q_\infty S}$
C_{LMAX}	Maximum Lift Coefficient
C_D	Drag Coefficient, $\frac{D}{q_\infty S}$
C_M	Moment Coefficient, $\frac{M}{q_\infty S c}$
C_p	Pressure Coefficient, $\frac{p-p_\infty}{q_\infty}$
C_μ	Jet Momentum Coefficient, $\frac{\dot{m_j} v_j}{q_\infty S}$
$(\frac{L}{D})$	Conventional Aerodynamic Efficiency
P_c	Power Coefficient, $\frac{L}{q_\infty S V_\infty}$
$(\frac{L}{D})_c$	Corrected Aerodynamic Efficiency for CFJ Airfoil, $\frac{L}{D+P/V_\infty} = \frac{C_L}{C_D+P_c}$
$(\frac{C_L^2}{C_D})$	Productivity Efficiency Coefficient
$(\frac{C_L^2}{C_D})_c$	Corrected Productivity Efficiency Coefficient for CFJ Airfoil
∞	Free Stream Conditions

I. Introduction

I.A. Wingtip Vortices

There are many compelling reasons to improve the understanding of the wingtip vortex rollup process. Some researchers study the process to augment tip vortex propagation mitigation strategies in an effort to increase airport capacity and reduce aircraft spacing and following distances around congested airports. There is another contingent of researchers who believe that the energy contained within the wingtip vortex can be recovered through mechanical means (winglets, turbines, etc). Yet others study the propagation of the vortex in the wake in an effort to leverage the vortex for increased lift and reduced lift induced drag (formation flight). There is, additionally, a splinter faction of researchers looking for a complete accounting of how parasite and lift induced drag are balanced in three-dimensional wings in a fluid mechanical sense. The present work is inspired by the last research area. This balance fundamentally determines the maximum lift to drag (L/D) ratio angle of attack. Practically speaking, this maximum L/D angle of attack occurs at angles of attack of little practical utility as they drive the cruise speed considerably slower than most airplanes are required to travel. Thus, by better understanding this parasite/lift induced drag tradeoff in a fluid dynamic sense, it may be possible to influence the angle of attack where maximum lift to drag occurs and nudge it towards a more practicable value. In a theoretical sense, Batchelor's[1] description of the wingtip vortex roll-up process includes the relationship between the azimuthal velocity and the wingtip vortex core axial velocity. As viscosity in the wake of the wing reduces the azimuthal velocity (primarily in the outer core) a positive pressure gradient results, consequently affecting a loss of axial momentum in the wingtip vortex core. The asymptotic variation of the axial velocity defect at the vortex center is given by Batchelor as,

$$u = x^{-1} log(x) \tag{1}$$

where u is the core axial velocity of the wingtip vortex and x is the distance downstream. Batchelor also included the drag associated with the core of the trailing vortex. The drag was expressed as an integral over the cross-stream plane independent of the downstream distance.

Brown[2] provided a relation that included the functional dependency between the axial core velocity and the link between the profile drag and the lift induced drag. The development of the turbulent core as

a function of downstream distance depends on the axial flow tied to the profile drag of the wing and that of the rotating flow. Brown translated pressure equations for axisymmetric swirling flows as,

$$\Delta p = -\rho U u - \frac{\rho V_t^2}{2} - \Delta H \tag{2}$$

$$\Delta p = -\int_r^\infty \frac{\rho V_t^2}{r} dr + c \tag{3}$$

Where Δp is the pressure increment above ambient pressure, ρ is the fluid density, ΔH is the total head loss, V_t is the azimuthal velocity, and c is a zero to first order constant. Brown related ΔH and profile drag through the axial momentum assuming that the entire wing wake rolls up with the wingtip vortex. When this relation is applied, axial core flow and its direction are the results. Brown concluded that the vortex axial flow formed at the vortex center may exhibit wake-like (less-than the freestream) or jet-like (greater than the freestream) core axial flow depending on the ratio of profile drag to the induced drag under a given set of conditions.

Anderson and Lawton[3] observed a relationship between maximum aerodynamic efficiency and the nature of the wingtip vortex. The axial velocity of the wingtip vortex core (streamwise aligned) transitions from jet-like (greater than freestream velocity) to wake-like (less than freestream velocity) in the vicinity of the the maximum L/D angle of attack. Lee & Pereira[4] and McAlister & Takahashi[5] experimentally confirms the observation. Memon & Altman[6] investigated the wingtip vortex roll up process as a function of angle of attack three chord lengths downstream of a Clark-Y wing. The authors found a discontinuity in the behavior of the vortex in terms of vorticity and dissipation (exergy) around max (L/D) angles. The discontinuity was attributed to the transformation of the wingtip vortex core axial flow from a wake-like to a jet-like profile in proximity to those angles of attack.[7] The wake-like axial core flow was observed at angles less than the angle of attack associated with max (L/D) whereas the jet-like axial core flow was observed at angles greater than those associated with max (L/D). The nature of the physics associated with this axial core flow direction change and how it correlates to the point of maximum aerodynamic efficiency has yet to be exhaustively investigated.

Devenport et al.[8] showed that the wing wake was indeed rolled up in the vortex by observing fluctuating quantities associated with the spiral motion. Gunasekaran & Altman[9] quantified the changes in the turbulence character in free shear layer of the wake of a flat plate across the span. The authors showed that the wingtip vortex moves above the free shear layer with increasing angle of attack. At higher angles of attack, the wingtip vortex is fully separated from the free shear layer. Moreover, a transfer of momentum from the free shear layer to the wingtip vortex was evident when transition was forced using a boundary layer trip. Subsequently, Gunasekaran and Altman[9] studied the nature of this interaction in greater detail. Both Batchelor's and Brown's models were found to deviate from the experimental data due to complex interaction with the wing wake free shear layer. And in the final paper in the series, Memon and Altman[10] included results that elucidated the magnitude of the opposing cross-stream flow through the wing wake free shear layer as being on the order of 10% of the freestream.

The concept behind the fluid dynamics analogy for the balance between the lift induced drag and the parasite drag can be explored further by studying the interaction between the wingtip vortex and the free shear layer. The coflow jet (CFJ) flow control wing provides a unique opportunity to study this dynamic interaction between the wing wake free shear layer and the wingtip vortex since its conceptual foundation should fundamentally alter this baseline wake shear layer and hence its influence on the wingtip vortex throughout the tip vortex formation process. These lingering questions form the underpinnings of the present investigation.

I.B. CFJ Active Flow Control

The Co-Flow Jet active flow control airfoil is a zero-net mass-flux(ZNMF) active flow control technique developed by Zha et al.[11–24] Applying this technique to a traditional airfoil provides the ability to increase lift and aerodynamic efficiency at low cost in energy expenditure. This low energy expenditure results from placing an injection slot near the leading edge and a suction slot near the trailing edge. Flow is injected near the suction peak and sucked at a position of higher [recovered] pressure. With the help of a pumping system inside the airfoil, the small amount of air drawn near the trailing edge is energized and is injected near leading edge tangent to the main local flow. The process does not add any mass flow and hence is a ZNMF system. This technique energizes the boundary layer, increases circulation, and reduces wake velocity deficit with reduced pressure drag.

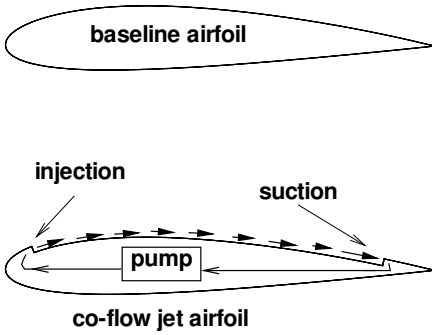

Figure 1: Schematic of Typical CFJ Wing

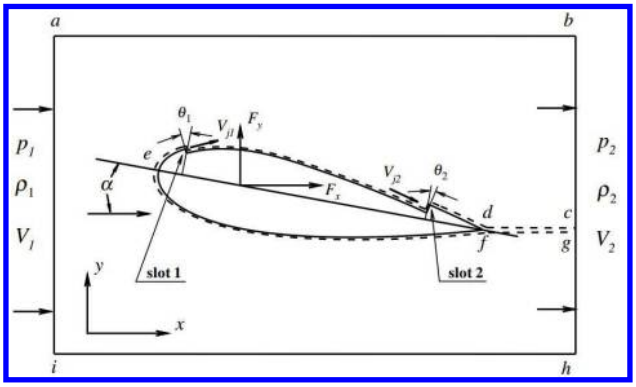

Figure 2: The CFJ airfoil control volume schematic.

II. Methodology

II.A. Numerical Approach

The numerical simulations were carried out using the in-house computational fluid dynamics (CFD) code Flow-Acoustics-Structure Interaction Package (FASIP). The Reynolds averaged Navier-Stokes (RANS) equations with the one-equation Spalart-Allmaras (SA)[25] turbulence model is incorporated in this application. The inviscid fluxes are evaluated using the low diffusion E-CUSP scheme suggested by Zha eta al.[26] with the 3rd order weighted essentially non-oscillatory (WENO) scheme. The 2nd order central differencing method is used to discretize the viscous terms. The implicit Gauss-Seidel (GS) line relaxation with two alternative sweeping directions is applied in each time step to achieve a fast convergence rate.[27] Parallel computing is implemented to save wall clock simulation time.[28] The code is extensively validated with various 2D and 3D flows including CFJ airfoil flows.[15,22,28–30]

II.B. CFJ Airfoil Parameters

II.B.1. Drag and Lift

Zha et al.[13] give the following formulations to calculate the lift and drag due to the CFJ reactionary forces for CFD simulation

$$R_x = (\dot{m}_j V_{j1} + p_{j1} A_{j1})\ cos(\theta_1 - \alpha) - (\dot{m}_j V_{j2} + p_{j2} A_{j2})\ cos(\theta_2 + \alpha) \tag{4}$$

$$R_y = (\dot{m}_{j1} V_{j1} + p_{j1} A_{j1})\ sin(\theta_1 - \alpha) + (\dot{m}_{j2} V_{j2} + p_{j2} A_{j2})\ sin(\theta_2 + \alpha) \tag{5}$$

where x and y represent the drag and lift directions, respectively, subscripts 1 and 2 represent the injection and suction, θ_i $(i = 1, 2)$ is the angle between the injection or suction slot surface and the line normal to the airfoil chord, and α is the AoA, as shown in Figure 2.

The total drag and lift of the CFJ airfoil can then be expressed as below

$$D = F_x - R_x \tag{6}$$

$$L = F_y - R_y \tag{7}$$

where F_x and F_y are the drag and lift force computed by the surface integral of pressure and shear stress. The corresponding drag and lift coefficients are expressed as follows

$$C_D = \frac{D}{\frac{1}{2}\rho_\infty {V_\infty}^2 S} \tag{8}$$

$$C_L = \frac{L}{\frac{1}{2}\rho_\infty {V_\infty}^2 S} \tag{9}$$

where ρ_∞ and V_∞ denote the free stream density and velocity. S is the wing reference planform area. For 2-D airfoil study, S denotes the planform area per unit span, which is equal to the airfoil chord length.

II.B.2. Jet Momentum

The jet momentum coefficient C_μ is a parameter used to quantify the jet intensity, which is defined as

$$C_\mu = \frac{\dot{m}V_j}{\frac{1}{2}\rho_\infty {V_\infty}^2 S} \tag{10}$$

where $\dot{m}$ is the injection mass flow rate, V_j is the averaged injection velocity at the injection slot opening.

II.B.3. Power Consumption

The CFJ can be implemented by mounting a pumping system inside the wing that withdraws air from the suction slot and blows it into the injection slot. The power consumption can be determined by the jet mass flow and total enthalpy change as follows

$$P = \dot{m}(H_{01} - H_{02}) \tag{11}$$

where H_{01} and H_{02} are the total enthalpy in the injection cavity and suction cavity, respectively. P is the power required by the pump. Introducing the pump efficiency η and total pressure ratio of the pump $\Gamma = \frac{P_{01}}{P_{02}}$, the power consumption can be expressed as

$$P = \frac{\dot{m}C_p T_{02}}{\eta}(\Gamma^{\frac{\gamma-1}{\gamma}} - 1) \tag{12}$$

where C_p is the specific heat constant for constant pressure and γ is the specific heat ratio for air. The power consumption can be further normalized as a power coefficient

$$P_c = \frac{P}{\frac{1}{2}\rho_\infty V_\infty^3 S} \tag{13}$$

II.B.4. Aerodynamic Efficiency

The conventional airfoil aerodynamic efficiency is defined as

$$(\frac{L}{D}) = \frac{C_L}{C_D} \tag{14}$$

For the CFJ airfoil, the ratio above represents the pure aerodynamic relationship between lift and drag. However, with the addition of energy through the pump, this would be an unfair representation of the actual system-level efficiency. Therefore, a method has been devised to take the energy consumption of the CFJ into account. Consequently, the approach taken herein is to modify the conventional aerodynamic efficiency by converting the power consumption into a corresponding drag force. The corrected aerodynamic efficiency is given as follows[18]

$$(\frac{L}{D})_c = \frac{L}{D + \frac{P}{V_\infty}} \tag{15}$$

in which the pump power consumption P is converted into a force $\frac{P}{V_\infty}$ added to the aerodynamic drag D. The formulation above can be further expressed using the non-dimensional coefficients C_L, C_D and P_c as

$$(\frac{C_L}{C_D})_c = \frac{C_L}{C_D + P_c} \tag{16}$$

Note that when the pumping power is set to zero, $(\frac{C_L}{C_D})_c$ returns to the conventional definition of the aerodynamic efficiency.

Another new parameter, the productivity efficiency introduced by Yang et al[23] will be utilized here as well. It describes the capability of an airplane to transport a gross weight with the maximum distance in cruise.

$$(\frac{C_L^2}{C_D})_c = \frac{C_L^2}{C_D + P_c} \tag{17}$$

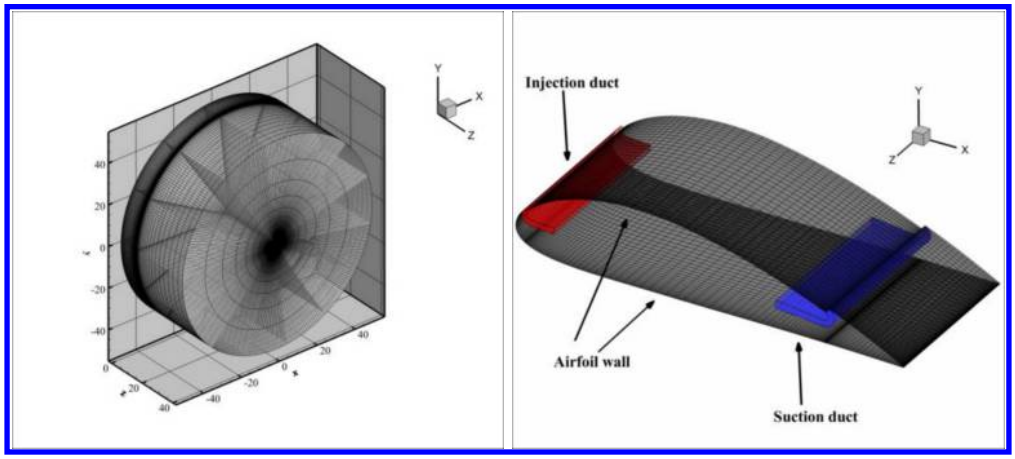

Figure 3: Computational Mesh

II.C. Boundary Conditions

A third order accuracy no slip condition is enforced on the solid surface. The computational mesh is shown in Figure 3 with O-mesh topology and the radial far-field boundary is located at 45 chord lengths. The spanwise far-field is located 30 chord lengths away from the wing tip. Total pressure, total temperature and flow angles are prescribed at the injection duct inlet, as well as at the upstream portion of the far field boundary. Constant static pressure is applied at the suction duct outlet as well as the downstream portion of the far field boundary. Symmetry boundary conditions are applied at the root of the wing. The cross-section faces of the CFJ ducts are meshed using "H" topology while the domains around the airfoil are meshed using "O" topology. The total mesh size is 10.5 million cells, split into 164 blocks for parallel computation. The first grid point on the wing surface is placed at $y+ = 1$. The mesh is refined along the wake and the tip vortex trajectory to resolve them in high resolution. The CFJ wing suction surface between the injection slot and suction slot is translated downwards by 1.5% chord. The injection slot size is 1.17%C and the suction slot size is 2.45%C. The baseline wing with the non-controlled NACA 6421 airfoil is also computed for comparison. Both the CFJ and baseline wing have an aspect ratio of 10. The freestream Mach number is 0.15 and the Reynolds number based on airfoil chord is 2.6 $\times 10^6$. Both wings have a rectangular planform with no sweep or taper. The same wing configurations are studied by Wang and Zha.[31]

II.D. Vortex Analysis

A widely used model for cross-stream plane oriented vortex characteristics and their variation with downstream distance was suggested by George Batchelor.[1] This model and its associated equations are now commonly referred to as the Batchelor Vortex. The Batchelor Vortex is often used in modeling airplane wakes and tip vortices. The model simplifies the Navier-Stokes equations using a boundary layer approximation. Notably, it also relates the azimuthal velocity distribution of the vortex with the axial velocity in the vortex core. The distribution of azimuthal velocity is described as follows:.[1]

$$(\frac{V_t(\eta)}{V_0}) = (1 + \frac{1}{2\alpha})\frac{1}{\eta}(1 - exp(-\alpha\eta^2)) \tag{18}$$

where $V_t(\eta)$ is the distribution of tangential velocity of the vortex, α is angle of attack in radians. V_0 is the maximum tangential velocity. $\eta = r/r_c$, where r is the radial location and r_c is the core radius of the vortex. The vortex core radius is collocated at the maximum tangential velocity radius.[32]

The azimuthal velocity is calculated as follows:

$$V_t = -w \times \cos(\Theta) + v \times \sin(\Theta) \tag{19}$$

Where, w is the velocity component in the spanwise direction, v is the velocity component in the vertical direction normal to the freestream. The vortex core axial velocity is the x-component velocity. The vortex is analyzed in various planes downstream of the wing. The CFD domain origin is the leading edge of the wing. Therefore at $X = 1.2$, the location refers to 0.2 chord lengths downstream of the trailing edge.

III. Results and Discussions

III.A. Validation and Mesh Refinement

The mesh refinement in this study was done to ensure sufficient resolution of the wingtip vortex downstream. The baseline mesh contains 3.5 million cells. The refined mesh done by Wang and Zha[31] proves the mesh independent results with 7 million cells. The mesh refinement was done by doubling the cell density in i,j, and k directions, respectively. While these results (see Table 1) show little variation in calculated coefficient of lift, drag, power and pitching moment, they are inadequate in resolving the wingtip vortex prolonged distances downstream. The refined mesh used in this paper doubles the size of the baseline mesh in the radial (η) direction and span-wise in the tip region (ζ). Similarly, the stream-wise mesh is also doubled near the trailing edge with the wake region alone containing nearly 2 million cells. The calculated force and moment coefficients are basically the same as the previous mesh refinement study, while the wingtip vortex and wing wake are resolved with much better resolution up to 30 chord lengths downstream toward the far field boundary.

Table 1: Mesh Independence Study for CFJ Wing at AoA = 5° and AR = 10

Case	AoA	$GridSize$	C_L	C_D	C_M	P_c
Baseline	5°	$281 \times 81 \times 121$	1.068	0.0458	−0.1623	0.0096
refined in-ξ	5°	$561 \times 81 \times 121$	1.065	0.0456	−0.1612	0.0093
refined in-η	5°	$281 \times 161 \times 121$	1.051	0.0444	−0.1571	0.0095
refined in-ζ	5°	$281 \times 81 \times 241$	1.069	0.0457	−0.1625	0.0096
Present Study	5°	$321 \times 161 \times 161$	1.068	0.0458	−0.1623	0.0096

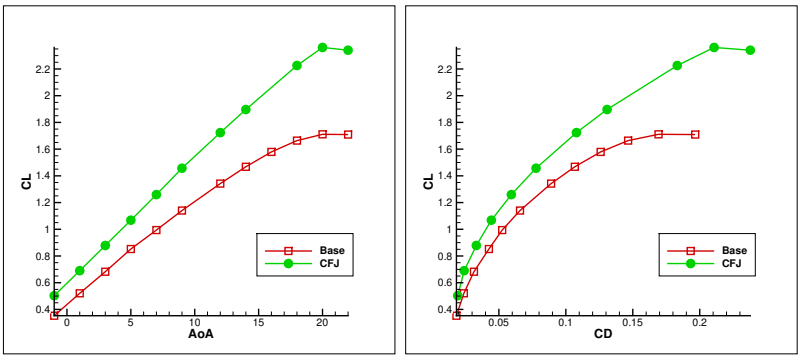

(a) **(b)**

Figure 4: a) CL v AoA and b) CL v CD for Baseline and CFJ Wings

The simulations are executed from $\alpha = -2°$ to 26° in 2° increments. Previous studies by Wang and Zha[31] are done with a fixed C_μ of 0.03. In this study, the injection total pressure corresponding to C_μ of 0.03 at an AoA of 5° is fixed while the AoA is varied. This is based on the more desirable control law to hold injection total pressure constant as indicated by Wang and Zha.[33] Holding injection total pressure constant enables a broader operating range than holding the injection momentum coefficient constant. The previous study[31] indicates that the AoA of 5° gives the best aerodynamic efficiency C_L/C_{Dc} for both the baseline and CFJ wing. Figure 4 presents the results of C_L vs AoA and the drag polar of the baseline and CFJ wing. The CFJ wing has the cruise lift coefficient increased significantly for all the angles of attack. Between 0 and 14° the average C_L increase for the CFJ wing is 28%.

Figure 5 shows conventional aerodynamic efficiency vs angle of attack for both the baseline and CFJ wings. The peak aerodynamic efficiency does not occur at $\alpha = 5°$, but at $\alpha = 2°$. This is different from the previous study,[31] which gives an AoA 5° as the peak aerodynamic efficiency for both the baseline and CFJ wing. The reasons appear to be twofold: 1) the AoA increment of 2° is smaller than the 5° increment in the previous study; 2) The wake and tip vortex are better resolved with the refined mesh. Fig. 6 shows the surface isentropic Mach number distribution at mid-span of the baseline wing and the CFJ wing at AoA=2° and 5°. It shows the lift loading is higher for the CFJ wing and provides support for the argument

that the CFJ generates supercirculation effects. These effects are evidenced by the change in pressure distribution over both the upper and lower surfaces. Fig. 7 are the Mach number contours at the mid-span for both wings. Fig. 8 is the Isentropic Mach number contours on the CFJ wing surface at an AoA of 5° with streamlines.

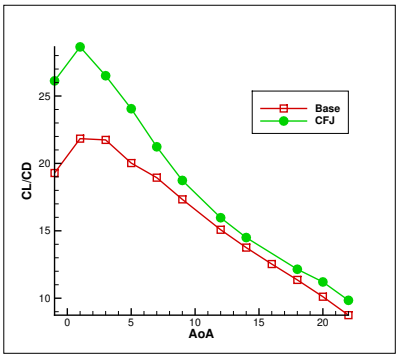

Figure 5: CL/CD for Baseline and CFJ Wings

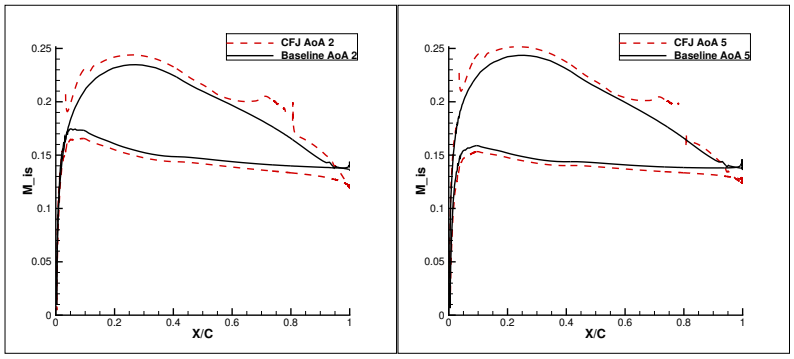

Figure 6: Isentropic Mach Distribution at Mid-span for CFJ and Baseline Wings for $\alpha = 2^\circ$ and $\alpha = 5^\circ$

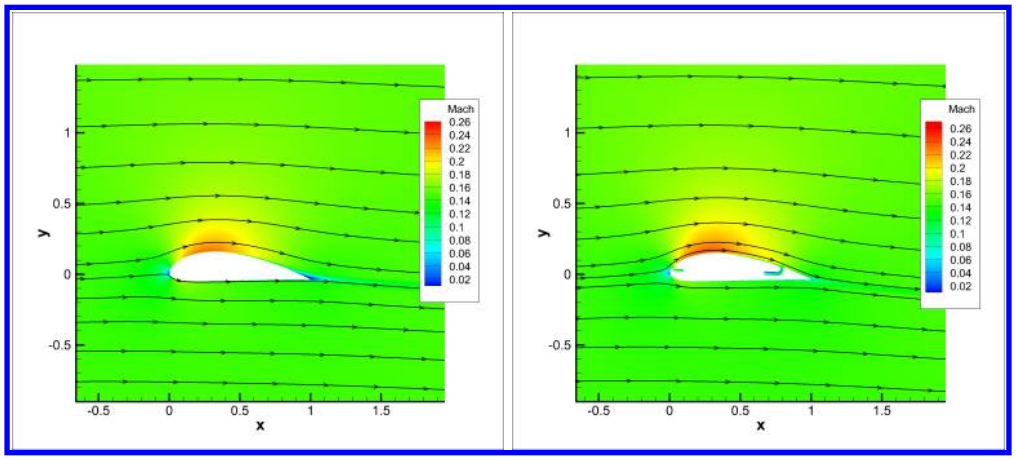

(a) Baseline $\alpha = 2^\circ$ **(b)** CFJ $\alpha = 2^\circ$

(c) Baseline $\alpha = 5^\circ$ **(d)** CFJ $\alpha = 5^\circ$

Figure 7: Mach Contours at mid-span for Baseline and CFJ Wing

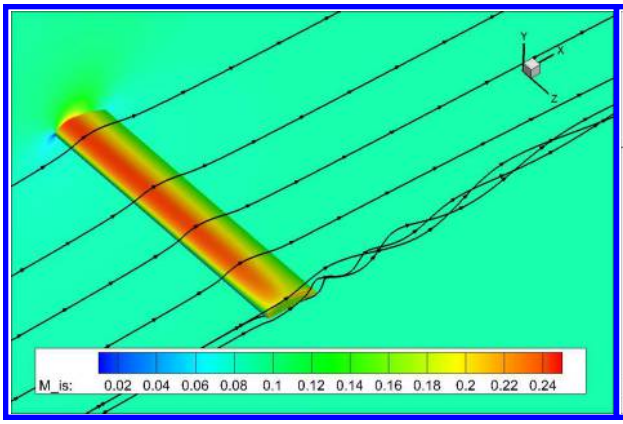

Figure 8: Baseline Wing AoA 5, Isentropic Mach Contours and Streamlines

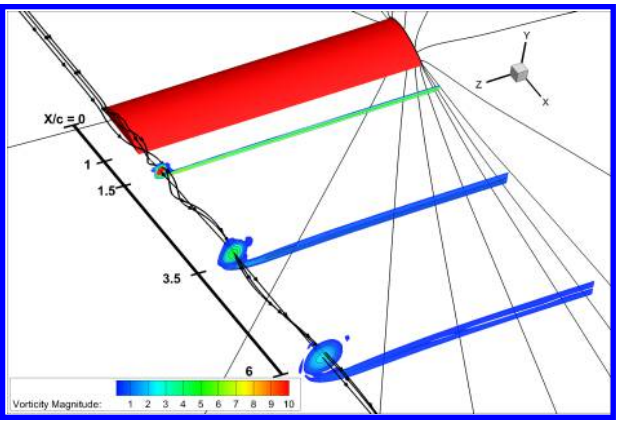

Figure 9: Baseline Wing AoA 5, Vorticity Contours and Streamlines

Figure 9 shows the normalized vorticity contours of the baseline wing at $\alpha = 5°$ and demonstrates that the tip vortex development and wing wake are very well resolved. The mesh topology is highlighted at the root of the wing. The blocks are more densely distributed in the wake region. Obviously the vorticity is high on the surface of the wing due to the wall boundary layer. The other vorticity peaks are at the vortex core and wake shear layer. The streamlines rewound from the wingtip go through the tip vortex core. The X-Plane slices of the vorticity contours downstream of the wing are at 0.5, 2.5, and 5 chord lengths downstream of the trailing edge, measured from the leading edge of the wing, X=1.5, 3.5, and 6. The subsequent plots and figures will be labeled based on distance from the leading edge.

III.B. Vortex Core Profile

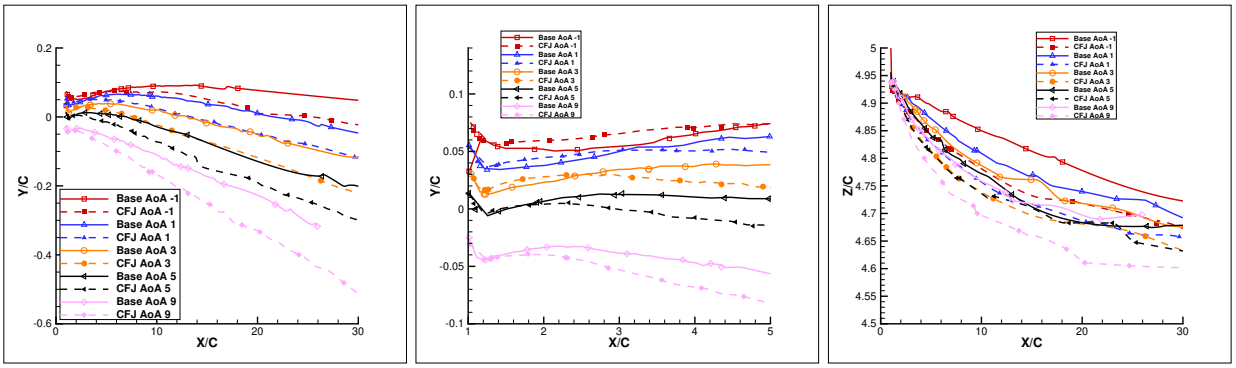

(a) **(b)** **(c)**

Figure 10: Baseline and CFJ wing tip vortex trajectory vs axial distance: a) vertical y-coordinates, b) Zoomed y-coordinates near the wing, c) Spanwise z-coordinates z(x)

Figure 10 shows the vortex core trajectory with the y and z coordinates along the axial distance downstream of the wing trailing edge. The y-origin point (y=0, z=0) is located at the wing root leading edge. The calculated trajectories of the tip vortices show that the vortex initially rises and remains above the wing at low AoA as shown in Fig. 10 (a) and (b). The tip vortices move to lower position downstream and go beneath the wing at high AoA. This is because that a higher AoA has a greater lift, stronger tip vortex and downwash. For the AoA of 9°, the vortex core drops 40% chord distance below the wing at the 30 chord length downstream location. Fig. 10(c) shows the spanwise position of the tip vortex trajectory, which moves toward the root of the wing for all AoAs. It is because of the "inner wash", which is the spanwise velocity pointing to the root due to the roll up of the tip vortex. The higher the AoA, the larger the inner wash. For the CFJ wing at an AoA of 9°, the tip vortex moves toward the root by a 40% chord distance at the 30 chord length downstream location, similar to the vertical distance that the vortex moves downward. These trajectories are used to determine the vortex core in order to conduct the analysis in the following sections.

III.C. Vorticity Magnitude

Figure 11 shows the vorticity distribution for the baseline and CFJ wing along the radius across the vortex core at 0.5 and 3 chord lengths downstream at AoAs of 1° and 5°, which are below and above the peak L/D point. The radius (z) is normalized by the radius of the local vortex core, Zc, which is defined to be located at the peak tangential velocity. At an AoA of 1°, the maximum vorticity of the CFJ wing at the vortex core is greater than the baseline wing as shown in Fig. 11 (a) and (b), which is attributed to the higher lift coefficient shown in Fig 4. However, at an AoA of 5° and 9°, the value for maximum vorticity is about the same for the CFJ wing and baseline wing. This occurs even though the lift coefficient at an AoA of 9° is higher than that at an AoA of 5° and the CFJ wing's lift coefficient is higher than that of the baseline wing at the same AoA (Fig 4). This is because the vortex core size is increased (at constant rotation rate) and the overall integral of the vortex circulation will be larger to match the higher lift coefficient. Caution should be exercised in extrapolating the vorticity to circulation since the results in Fig. 11 is the vorticity distribution along the radius and are not circumferentially averaged. Fig. 11 (c) is the vorticity distribution normalized by their respective maximum vorticity. They collapse very well and demonstrate a similarity solution.

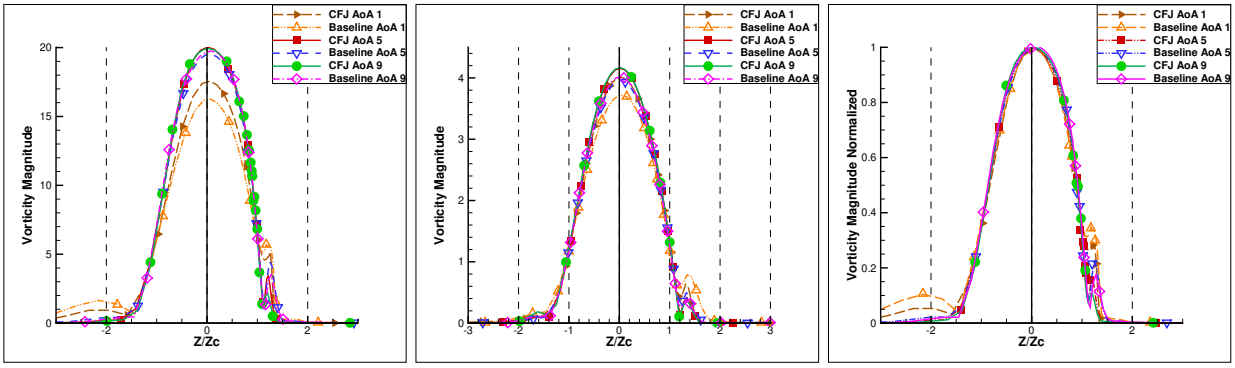

(a) 0.5 Chord Lengths Downstream **(b)** 3 Chord Lengths Downstream **(c)** 0.5 Chord Lengths Downstream, Normalized by Peak Magnitude

Figure 11: Vortex Core Axial Vorticity Magnitude Profile

Figures 12, 13, and 14 are the comparison of vorticity contours at $\alpha = 1°$, 5°, and 9° for the baseline and CFJ wings at 0.2, 0.5, 3.0 and 5.0 chord lengths downstream of the trailing edge. The vorticity contours and the dimensions are shown with the same magnitude scale for all the cases to facilitate direct comparison. The tip vortex and free shear layer size grow and the strength decays with the vortex propagating downstream. The vorticity magnitude is a little higher for the CFJ wing tip vortex, in particular at the low AoA of 1° as shown in Figure 11. The tip vortex size of the CFJ wing is also a little larger than that of the baseline wing for all the axial locations due to the higher lift coefficient. For all the AoAs, the CFJ wing free shear layer is thinner, with smaller vorticity magnitude than the baseline wing due to the coflow jet energizing the boundary layer and making the wake thinner with a shallower velocity deficit. The outcome is that the pressure/form drag of the CFJ wing is less than that of the baseline wing. In addition to the shear layer size difference, the shear layer location of the CFJ wing is also always lower than that of the baseline wing. This is because the CFJ wing has high circulation, which drives the shear layer more downward. It has been shown in other studies that the free-shear layer and wingtip vortex are deflected downwards at different rates .[32] These rates are proportional to the angle of attack of the wing but are not the same between the wing wake free shear layer and the wingtip vortex. This interaction drives the behavior of the evolution of the wingtip vortex roll-up process and could potentially hold the key to better understanding the relationship between lift induced and parasite drag.

Fig. 15 to 17 are the comparison of streamwise vorticity contours at $\alpha = 1°$, 5°, and 9° for the baseline and CFJ wings at 0.2, 0.5, 3.0 and 5.0 chord lengths downstream of the trailing edge, corresponding to Figures 12 to 14 at the same condition and location. The tip vortex is clockwise rotating seeing from downstream as shown in Fig. 15 to 17. Again, the CFJ wing has stronger core vorticity intensity than the baseline. Surrounding the core vortex with negative streamwise vorticity(in blue and green), the vorticity reaches zero at the edge of the vortex core (in yellow) because the azimuthal velocity varies from zero at the center of the core to the maximum at the edge of the vortex core. In other words, the size of the vortex core is identified by the zero vorticity ring(in yellow), beyond which the vorticity reverses the sign (in

red and pink) because the azimuthal velocity decreases due to decaying radically outward. The azimuthal velocity variation can be clearly seen in Fig. 25 to be described later. The tip vortex remains rotating in the clockwise direction radially even though the vorticity reverses the sign.

Fig. 15 to 17 also indicates that the CFJ wing has stronger streamwise vorticity in the free shear layer near the tip. This is opposite to the weaker spanwise vorticity of CFJ wing due to the energized boundary layer.

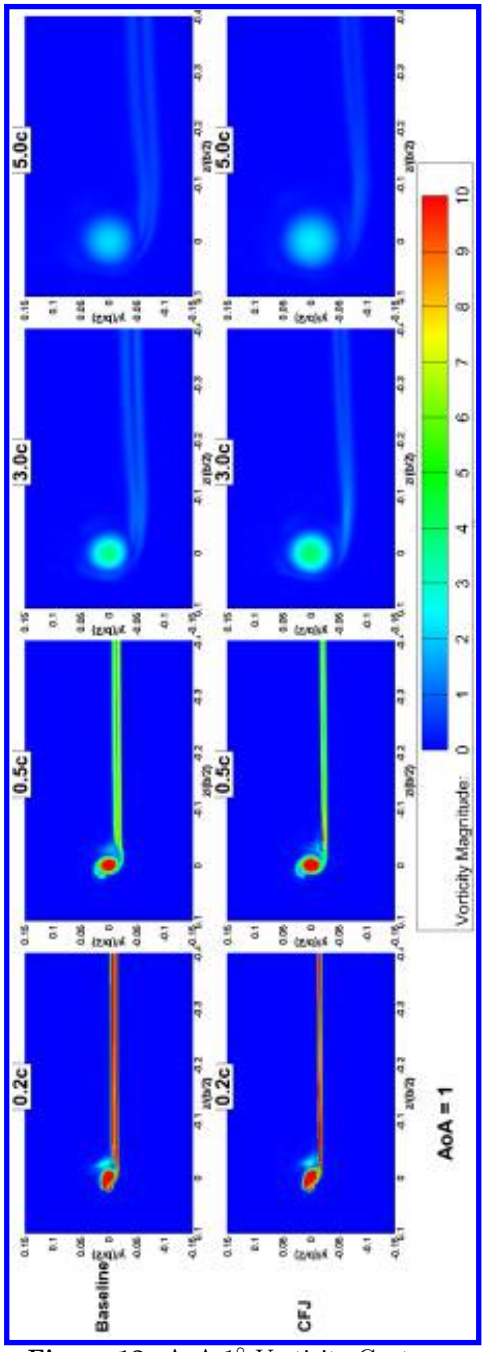

Figure 12: AoA 1° Vorticity Contours. 0.2, 0.5, 3.0 and 5.0 chord lengths downstream

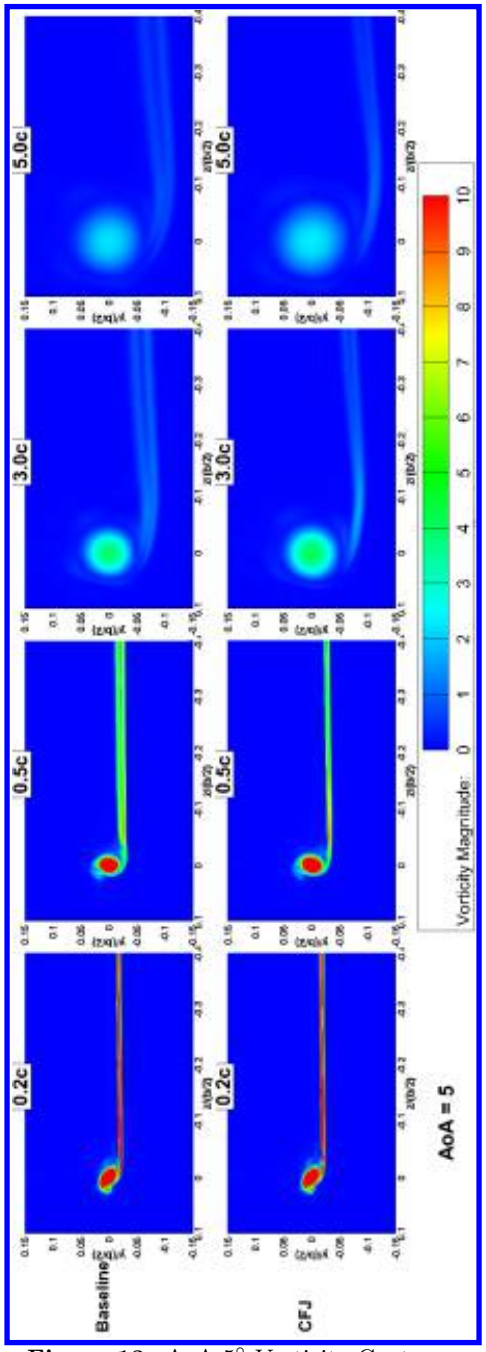

Figure 13: AoA 5° Vorticity Contours. 0.2, 0.5, 3.0 and 5.0 chord lengths downstream

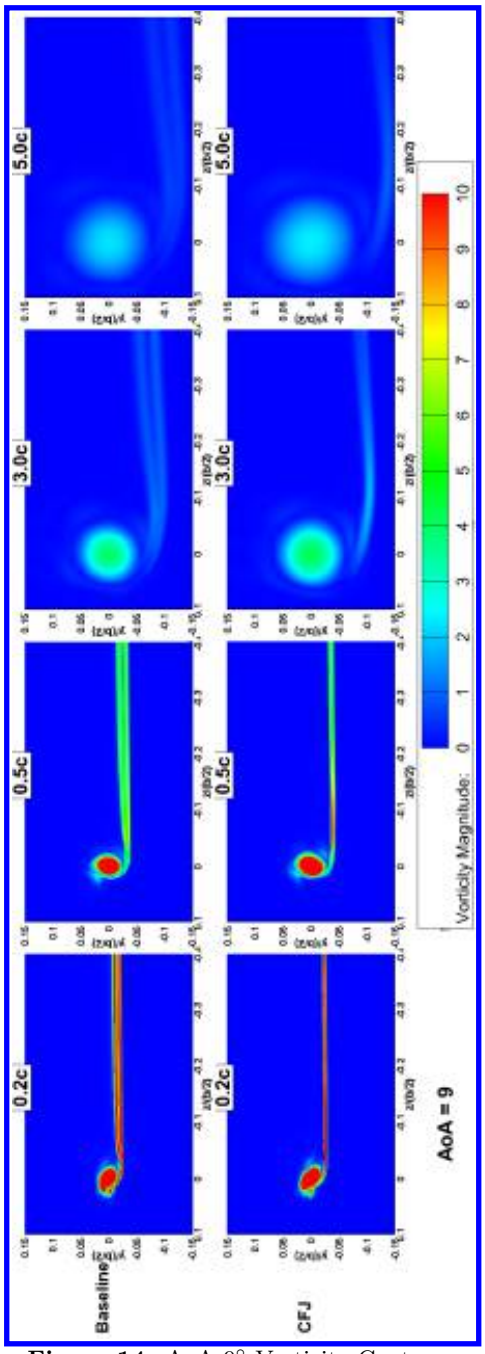

Figure 14: AoA 9° Vorticity Contours. 0.2, 0.5, 3.0 and 5.0 chord lengths downstream

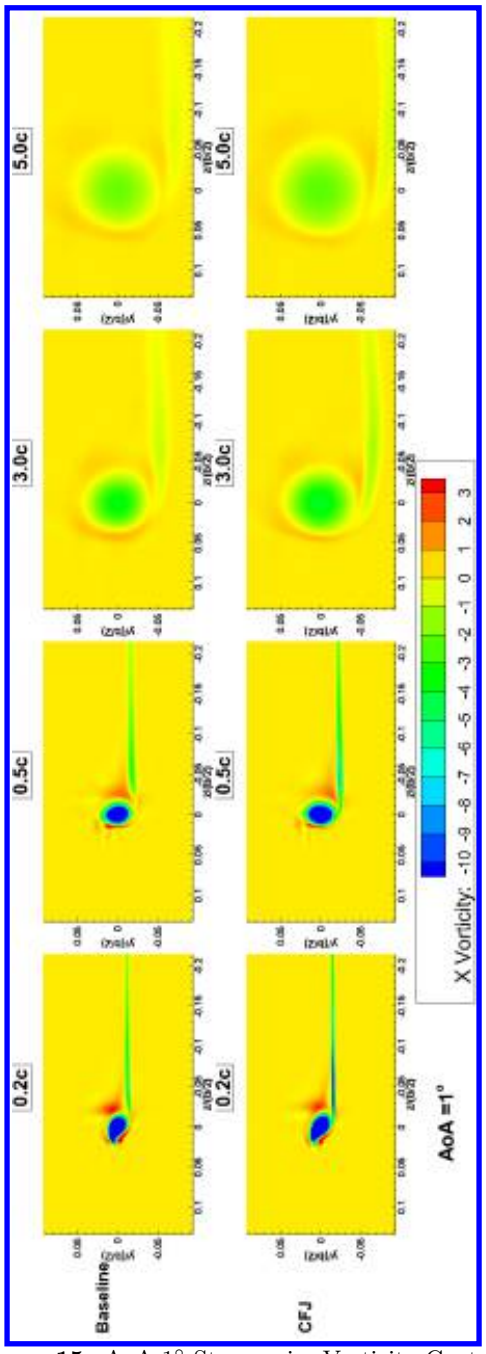

Figure 15: AoA 1° Streamwise Vorticity Contours 0.2, 0.5, 3.0 and 5.0 chord lengths downstream

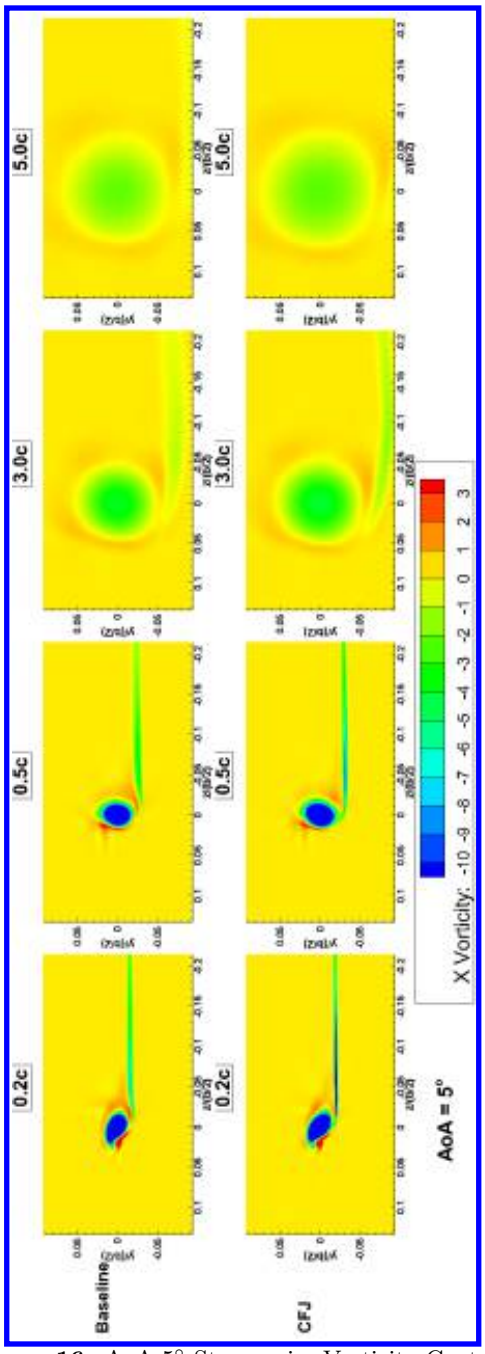

Figure 16: AoA 5° Streamwise Vorticity Contours 0.2, 0.5, 3.0 and 5.0 chord lengths downstream

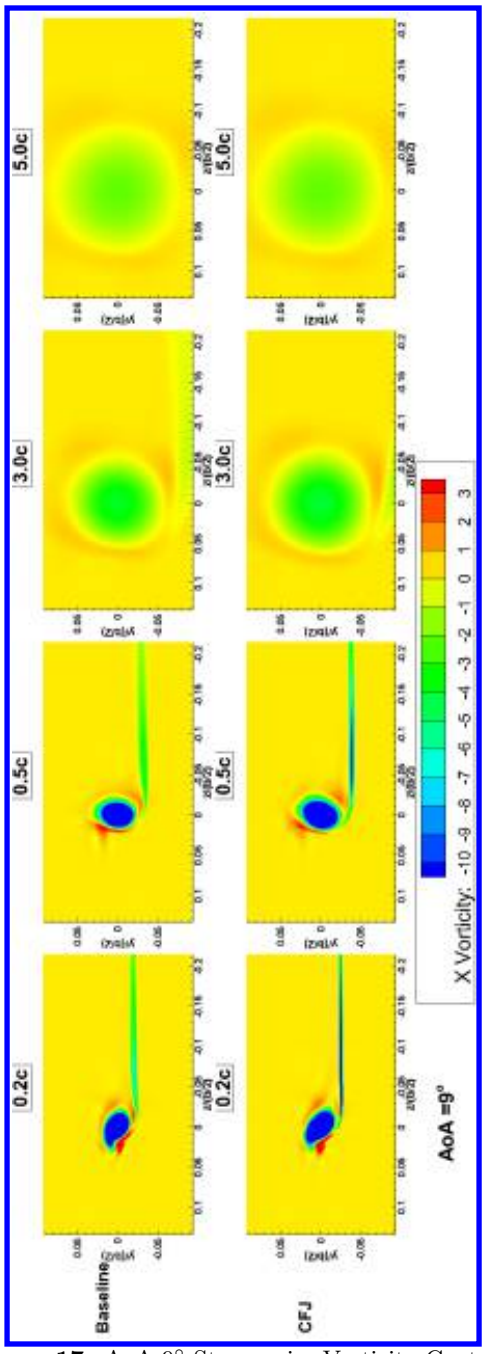

Figure 17: AoA 9° Streamwise Vorticity Contours 0.2, 0.5, 3.0 and 5.0 chord lengths downstream

III.D. Axial Velocity

As mentioned earlier when describing the relationship between aerodynamic efficiency and angle of attack, the angle corresponding to peak L/D may occur in proximity to the crossover point where the axial core velocity transitions from wake-like to jet-like. In the present study, this transition should happen between $\alpha = 1°$ and $\alpha = 3°$. Figure 18 presents the axial velocity distribution across the vortex core along the radius at three locations of 0.2 chord, 0.5 chord and 3 chords downstream of the wing trailing edge. In the near wake of the wing in Figure 18a, at 0.2 chord lengths from the trailing edge, the jet like behavior of the core of the forming vortex is only seen at the higher angle of attack of 12°. This effect is enhanced with the CFJ wings at the same angle of attack, which generates higher lift coefficient as well as higher induced drag coefficient. At the 0.2 chord length downstream location, both AoA of 1° and 5° show wake-like behavior, which is below and above the peak L/D point. The results of this study do not show the switch

from the wake-like and jet-like axial velocity profile at the peak L/D for either the baseline and CFJ wing. At the edge of the vortex core, where $z/z_c = 1$, jet-like behavior is seen at an AoA of 5°. Although the bulk core flow is not jet-like, this surplus along the outer boundary of the vortex provides some insight into the evolution of the transition from wake-like to jet-like behavior and the dynamic exchange between the wing wake free shear layer and the wingtip vortex throughout the near-wake vortex formation process. At the 0.5 chord lengths location, the jet-like velocity profile of AoA 12° is diffused and the wake defect becomes deeper and more characteristically formed for the AoA of 1° and 5°. At the 3 chord lengths downstream, all the vortex core axial velocity profiles are wake-like. Such a velocity profile variation is consistent with the analysis of Batchelor and Brown:[1,2] A higher lift coefficient with a higher induced drag creates a higher vortex core axial velocity at the near trailing edge area. With the core vortex size growing downstream, an adverse pressure gradient is developed along the vortex core trajectory and the core axial velocity decays. Eventually, all the axial velocity profiles are wake-like at downstream locations when the vortex core pressure is approaching the ambient pressure to reflect the drag of the wing.

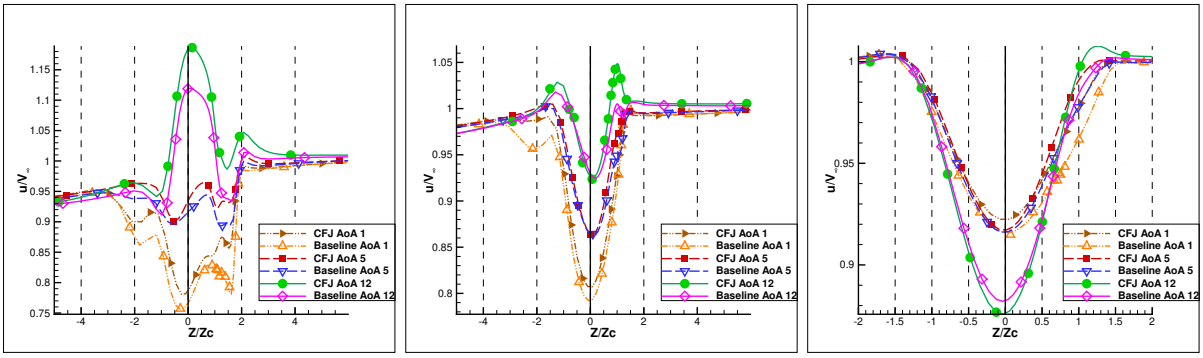

(a) 0.2 Chord Lengths **(b)** 0.5 Chord Lengths **(c)** 3 Chord Lengths

Figure 18: Vortex Core Axial Velocity Profile

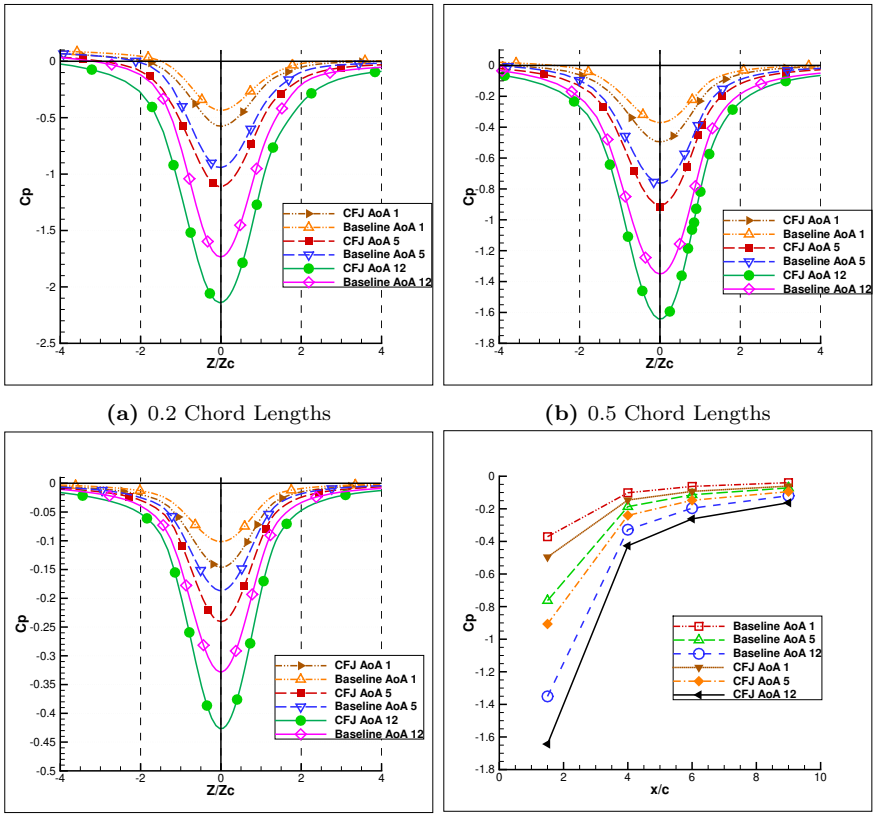

(a) 0.2 Chord Lengths **(b)** 0.5 Chord Lengths

(c) 3 Chord Lengths **(d)** Peak C_P vs Downstream Location

Figure 19: Vortex Core C_P Profile

Fig. 19 (a), (b), (c) are the pressure coefficient distribution across tip vortex core corresponding to Fig. 18 for the two wings at AoAs of 1°, 5°, and 12° and at downstream location of 0.2 chord, 0.5 chord and 3 chords. Fig. 19 (d) is the peak pressure coefficient streamwise distribution along the vortex core center trajectory. The pressure at the vortex core initially at 0.2 chord lengths downstream is substantially lower than the ambient pressure due to the vortex rolling up with very small core size, high vorticity, and high core axial velocity. A higher AoA gives lower vortex core pressure due to higher lift. For the CFJ wing, the core pressure is always lower than that of the baseline wing due to the higher lift coefficient and stronger tip vortex intensity. For both wings at all the AoAs , the adverse pressure gradient is developed along the vortex core trajectory due to the increasing size of the vortex core as indicated by Batchelor.[1] The adverse pressure gradient decreases the core axial velocity rendering all profiles wake-like. The higher the lift coefficient, the greater the adverse pressure gradient, the greater the vortex size growth rate.

Figs. 20, 21, and 22 are the axial velocity contours at the locations of 0.2 chord, 0.5 chord, 3.0 chords and 5.0 chords downstream of the wing trailing edge for the two wings at the AoAs of 1°, 5°, and 9° respectively. Comparing the plot in Figure 18 with the axial velocity contours of Figs. 20-22, it can be seen that the profile is wake-like at low angles of attack. This is true at $\alpha = 1°$ even for the CFJ wing. At $\alpha = 5°$ there are clearly visible jet-like contours, where velocity is above the freestream. At the edge of the vortex, where the free-shear layer is rolling-up and the tangential velocity is at a maximum, there is a significant region of high axial velocity. This means that the tip vortex has its highest total velocity at the edge of the vortex. However, the lowest pressure is located at the very center of the vortex cores instead of at the edge as indicated by Fig. 19 in a symmetric manner. It does not show the asymmetry of the axial velocity at the 0.2 chord location displayed in Fig. 18(a). From the flow topology in the region of the wingtip vortex, the regions of greatest velocity surplus result from the region sandwiched between the coherently formed tip vortex and the feeding shear layer. At $\alpha = 9°$, this region is much more pronounced. Also at this angle of attack, the jet is evident 0.2 chord lengths downstream.

Figures 23 and 24 show vertical slices of the axial velocity profile taken one chord length downstream at the wing tip and mid-span. At the wing tip, the tip vortex has primarily a wake-like profile, accompanied by a region of jet-like profile at the lower edge of the vortex due to the sandwiched high speed layer wrapping the tip vortex by the feeding wing wake free shear layer. The CFJ wing tip vortex has a higher jet velocity peak than the baseline wing. Additionally, there is a notable difference in the nature of the distribution of axial velocity through the shear layer region between the baseline and CFJ cases for a given angle of attack. At the mid-span, the wake has a typical velocity deficit profile. But the CFJ wing has a much shallower wake defect due to the added energy from the CFJ. Also, the wake position is lower with increasing AoA due to the higher lift coefficient and circulation. The CFJ drives the wake and the tip vortex position even lower.

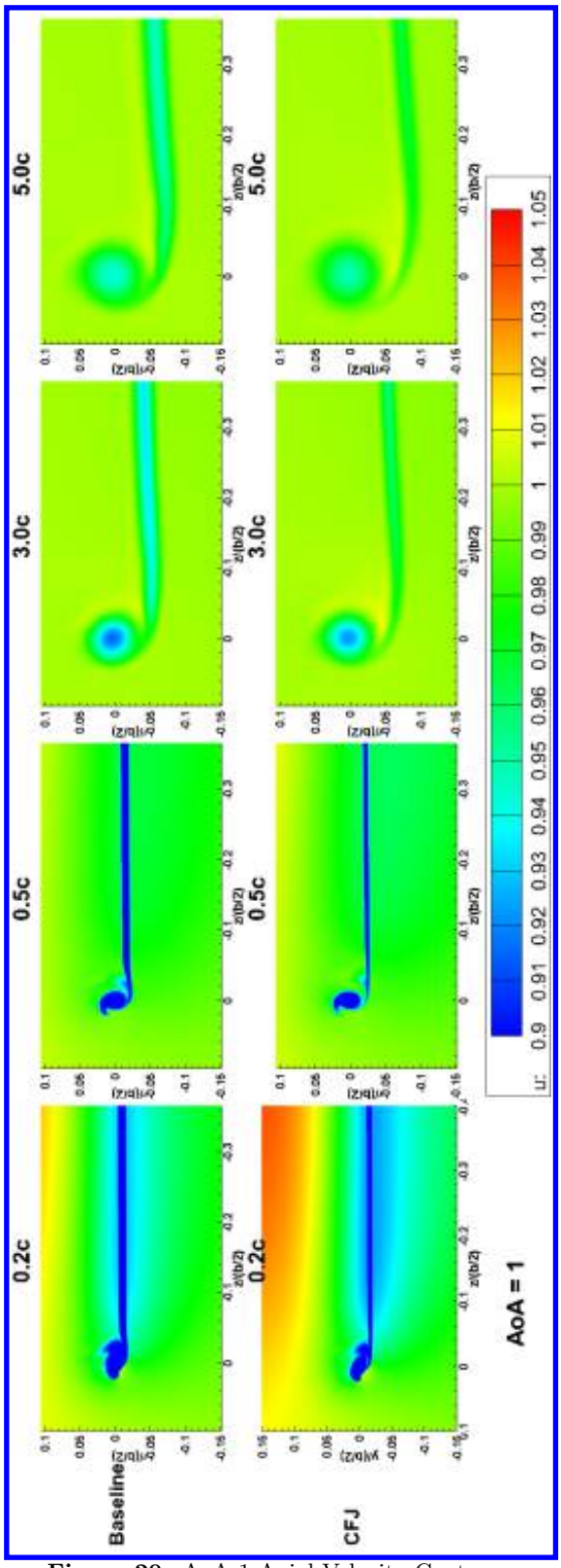

Figure 20: AoA 1 Axial Velocity Contours. 0.2, 0.5, 3.0 and 5.0 chord lengths

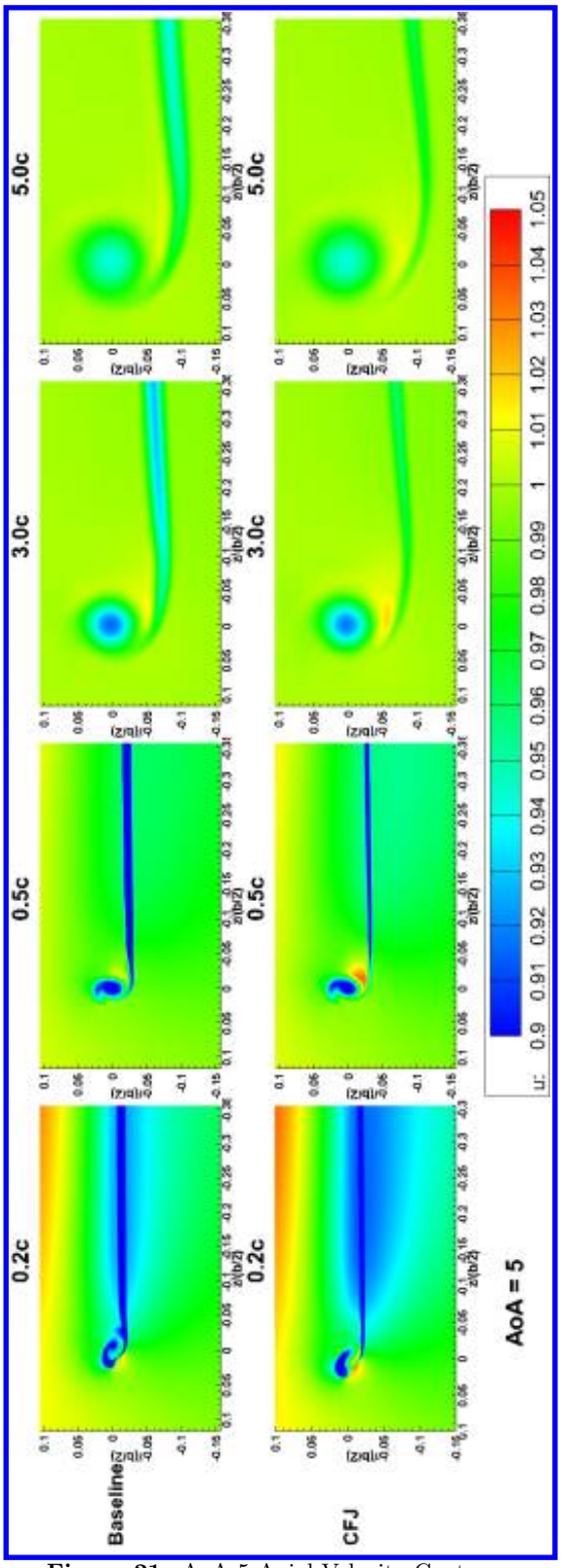

Figure 21: AoA 5 Axial Velocity Contours. 0.2, 0.5, 3.0 and 5.0 chord lengths

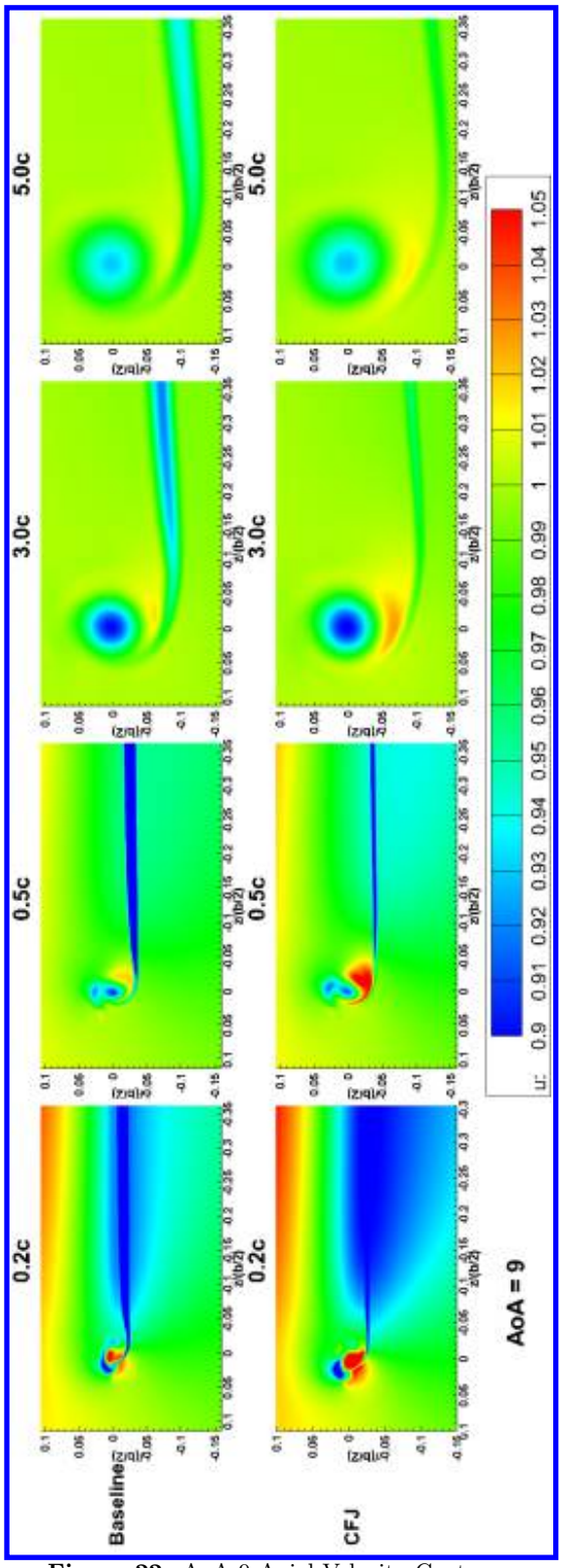

Figure 22: AoA 9 Axial Velocity Contours.
0.2, 0.5, 3.0 and 5.0 chord lengths

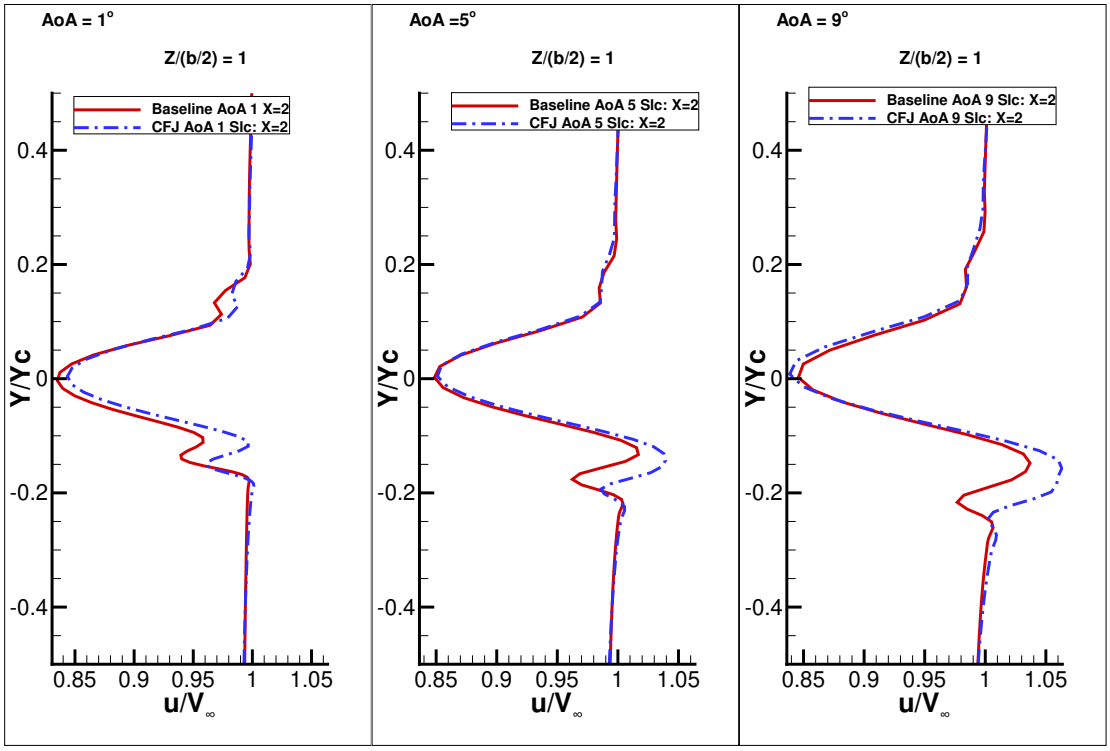

Figure 23: Vertical Slice 1 chord length downstream, Axial Velocity (u), 100% Span

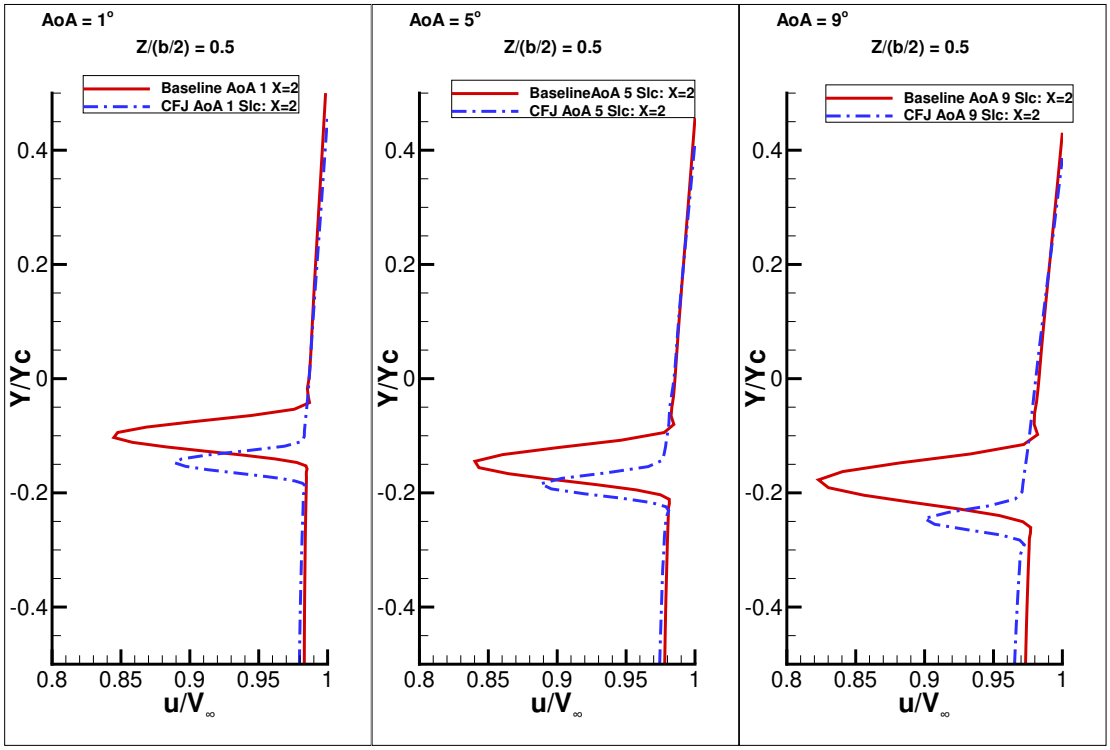

Figure 24: Vertical Slice 1 chord length downstream, Axial Velocity (u), 50% Span

III.E. Azimuthal Velocity

Figure 25 is the azimuthal (tangential) velocity calculated with Eq. (19) plotted against the normalized radius of the vortex core at the 0.5 and 2.5 chord locations downstream of the trailing edge. The Batchelor

vortex[1] defined in Eq. (18) at an AoA of 5° is plotted as a reference for comparison with the baseline wing. The azimuthal velocity at the inner core lines up fairly well between Batchelor's model and the CFD result for both the 0.5 and 2.5 chord locations, although the numerical result does show some asymmetry associated with plotting z/zc instead of r/rc. The CFD calculation shows the azimuthal velocity dissipates more quickly than the Batchelor model outside of the vortex core. This could be attributed to viscous dissipation when compared to the idealized model by Batchelor.[1] Batchelor's vortex model predicts higher tangential velocity resulting in higher vortex core axial velocity. This is confirmed in the present study by comparing Fig. 18 and Fig. 25 at the 0.5 chord downstream position. At the vortex core of the CFJ wing, the tangential velocity is higher than that of the baseline wing (Fig. 25(a)) along with the axial velocity (Fig. 18(b)). In a previous study, the zero-lift angle of attack for the baseline wing was seen to be $-5°$. Interpolating based on this angle of attack, the difference in the azimuthal velocity magnitude from 1° to 5° nearly varies two times between $\alpha = -5°$ and 1°, boldly assuming $V_t = 0$ at $\alpha = -5°$. This makes the relationship between α and the peak averaged azimuthal velocity a predictable function as seen in Figure 26, which shows exceptional agreement between Batchelor's model and the CFD prediction for the baseline wing.

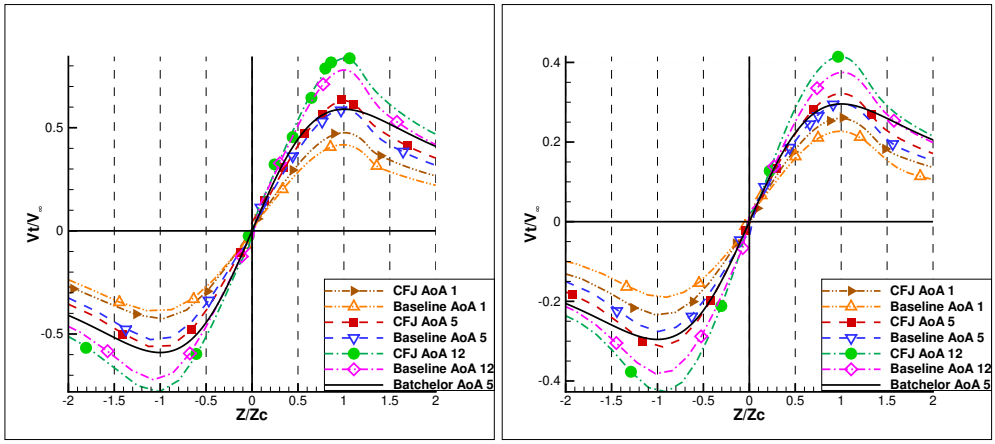

(a) 0.5 Chord Lengths Downstream **(b)** 2.5 Chord Lengths Downstream

Figure 25: Azimuthal velocity radial distribution, Vt vs Z/Zc

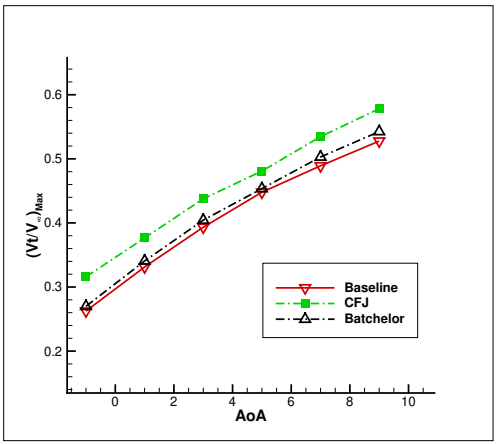

Figure 26: Comparison of the peak azimuthal velocity at different AoA at 1 chord length downstream of the wing.

III.F. Transverse Velocity (w)

The transverse velocity (z-component, spanwise velocity) contours in color imposed with the vorticity contour lines (black) are shown in Figs. 28, 29, and 30 for AoAs of 1°, 5° and 9° respectively. They show the tip vortex roll up field at 0.5 chord, 1 chord, 2 chord and 3 chord lengths downstream of the wing. The transverse velocity is negligible in most of the inner span and grows dramatically in the tip region due

to the roll up of the tip vortex. The roll up is emanated beneath the wing with the transverse velocity direction pointing outward (in red). The velocity direction is reversed when the flow is rolled up. Across the center of the tip vortex, there is a layer of quiescent transverse velocity sandwiched between the two areas with opposite transverse velocity direction. Two phenomena are observed by comparing the area of the transverse velocity field with the tip vortex sizes represented by the contour lines. First, for all the AoAs, the tip vortex size grows significantly with downstream vortex propagation, but the transverse velocity area remains relatively constant without much decay. Second, the area of significant transverse velocity is much larger than the tip vortex itself. This originates from the transverse velocity field being induced by the core of the tip vortex. This induction effect can radiate a large distance before it is dissipated by the the viscosity. The greater the strength of the vortex core, the larger the induced velocity area. This phenomenon can be observed in Figs. 28-30 as the area of transverse velocity for the CFJ wing is significantly larger than that of the baseline wing at the same AoA and downstream location. Similarly, higher AoA also induces a larger transverse velocity area.

Figure 27 shows the transverse velocity distribution along a spanwise line 10%C above and 10%C below the wing at the trailing edge. Fig. 27 indicates that the outward transverse velocity (positive sign) at the lower part of the vortex is substantially smaller than the inward transverse velocity (negative sign) due to the vortex rolling up effect. The maximum transverse velocity magnitude is up to 70-80% of the freestream velocity. As observed in Fig.27=Fig. 30, the CFJ wing tip vortex induces a larger transverse velocity than that of the baseline wing, so does the higher AoA.

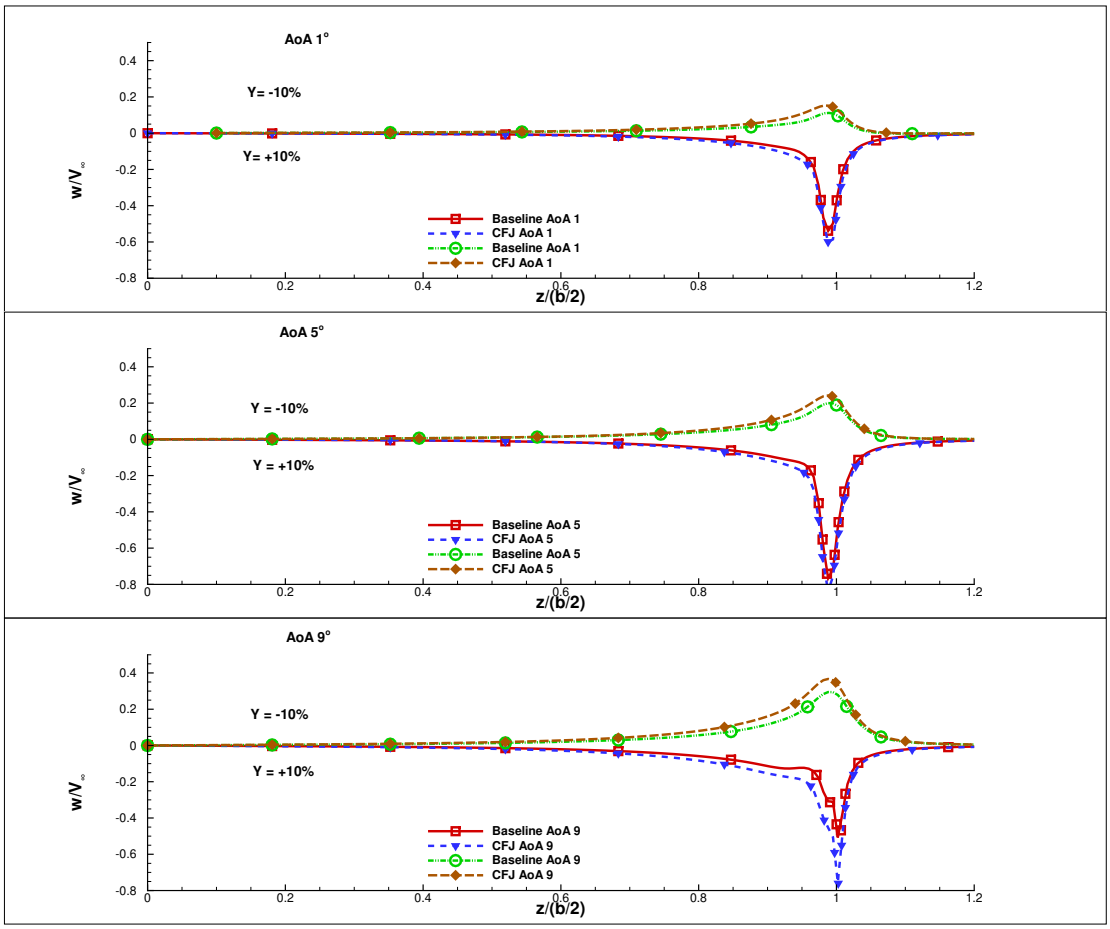

Figure 27: Horizontal Slice +10% and -10%, Cross-Plane Velocity (w), Normalized Span

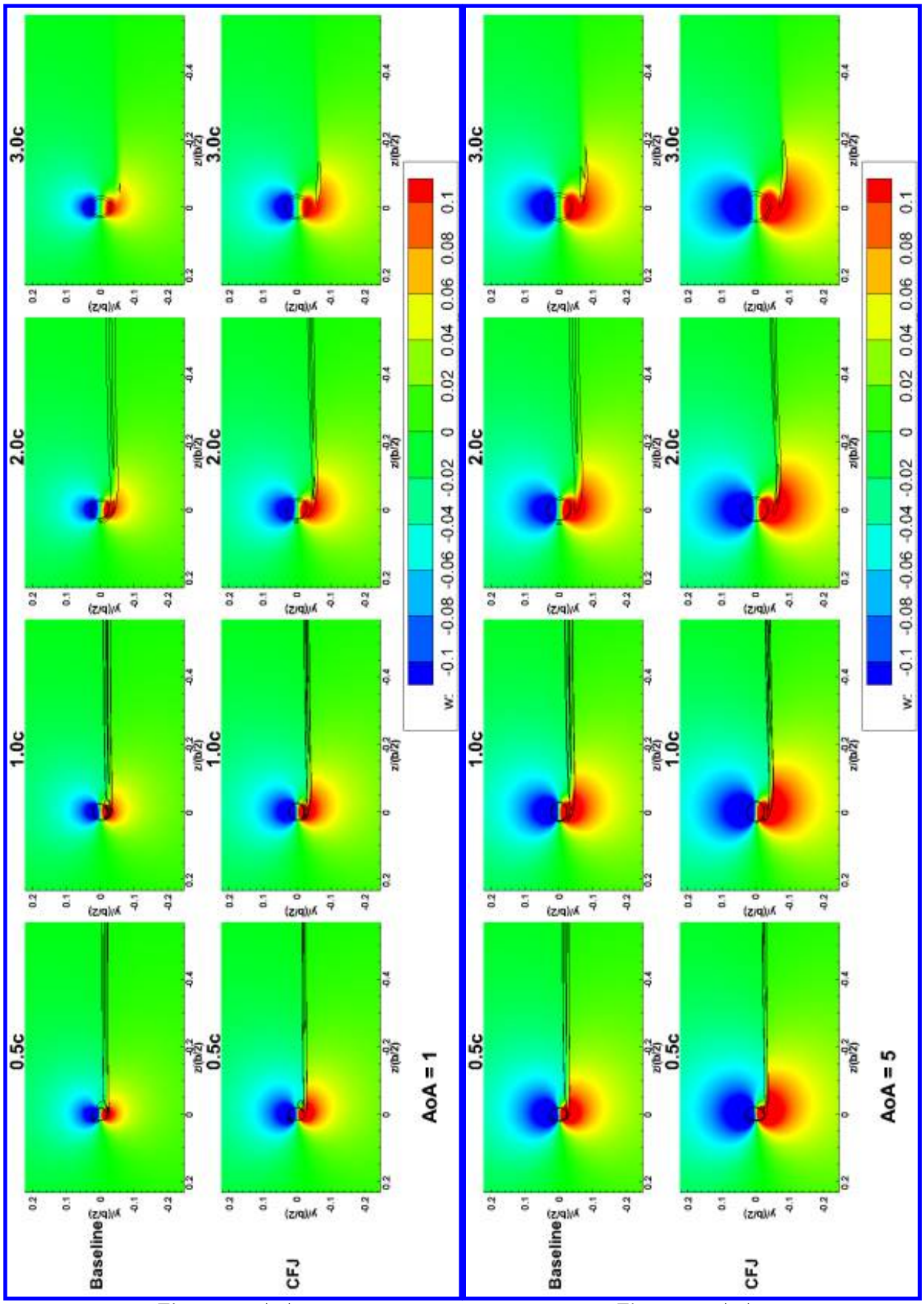

Figure 28: AoA 1
Cross-Plane Velocity(w) Contours
0.5, 1.0, 2.0 and 3.0 chord lengths

Figure 29: AoA 5
Cross-Plane Velocity(w) Contours
0.5, 1.0, 2.0 and 3.0 chord lengths

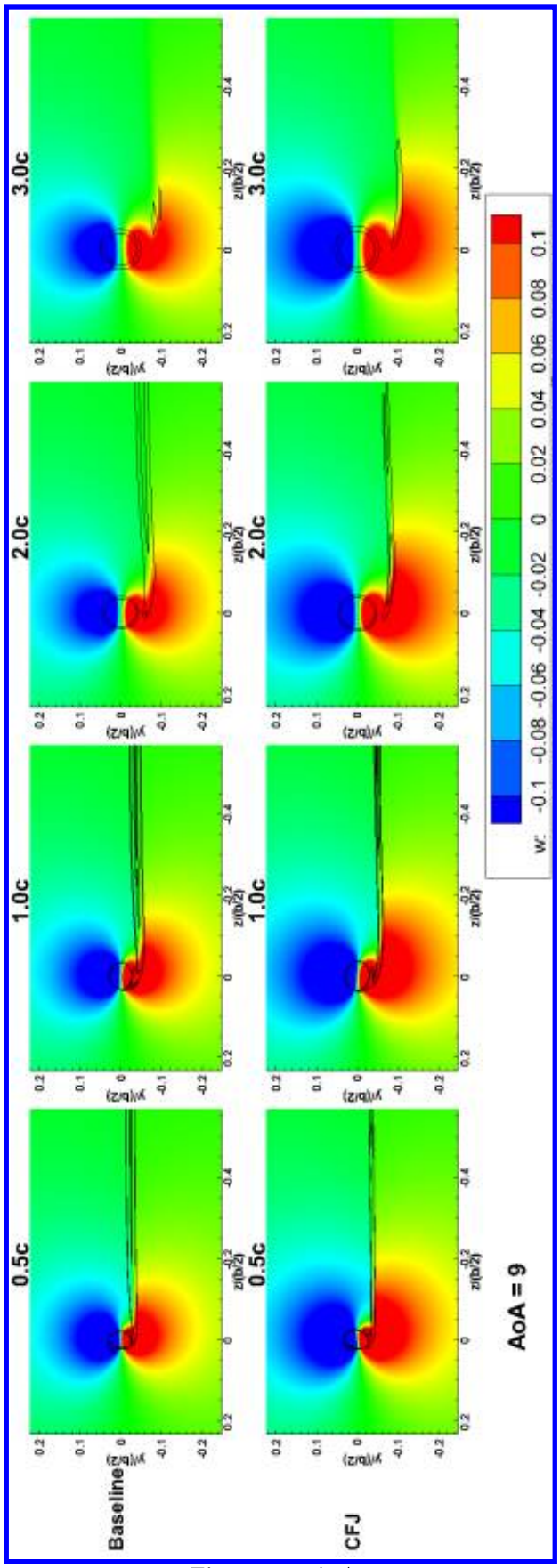

Figure 30: AoA 9
Cross-Plane Velocity(w) Contours
0.5, 1.0, 2.0 and 3.0 chord lengths

IV. Conclusion

This study examines a finite-wing with an aspect ratio of 10 and NACA 6421 airfoil section. Both a baseline wing and Co-Flow Jet Active Flow Control wing are studied. The total pressure that provides a C_μ of 0.03 at $\alpha = 5°$ is used as the injection slot boundary condition for each angle of attack. The peak aerodynamic efficiency (maximum lift-to-drag ratio) occurs between $\alpha = 1°$ and $\alpha = 2°$, across which the vortex core velocity remain mostly wake-like at the near wing region. However, the axial velocity at the vortex core increases with some jet-like axial velocity at the edge of the vortex when the AoA is at 5°. At high AoAs of 12°, the core axial velocity has a strong jet in the near wake region. With the tip vortex growing in size as it propagates downstream, an adverse pressure gradient is created as predicted by Batchelor's model and the axial velocity decreases to yield a uniquely wake-like profile. The intensity of the axial velocity profile is tied directly to the vortex strength: the greater the lift, the stronger the vortex intensity, the larger the induced drag, and the greater the axial velocity. This is consistent with Brown's analysis. The maximum azimuthal velocity of the vortex core is higher for the CFJ than the baseline wing at the same angle of attack due to the higher lift coefficient achieved by the CFJ augmented wing. The CFJ wing has a thinner free shear layer than that of the baseline wing due to energy added by the CFJ. However, the tip vortex strength of the CFJ wing is greater than that of the baseline wing. It is observed that the CFJ wing has greater free shear layer streamwise vorticity near the tip than the baseline wing at the same AoA. The azimuthal velocity profile agrees with Batchlor's model quite well. The CFJ wing always has greater azimuthal velocity at the same AoA due to the higher lift coefficient. It is observed that the area of the transverse velocity induced by the tip vortex is substantially larger than the size of the tip vortex. It also remains fairly constant propagating downstream while the tip vortex core size grows. In summary, although there are significant changes in magnitude between the CFJ and baseline cases across the conditions studied here, there are not fundamental differences in the flow topology.

V. Acknowledgments

The simulations are conducted on Pegasus supercomputing system at the Center for Computational Sciences at the University of Miami. The work is partially supported by the 2019 AFOSR Summer Faculty Fellowship Program.

The United States Air Force Research Laboratory(88th ABW) has evaluated this manuscript and designated it Approved for Public Release/Unlimited Distribution; Case #88ABW-2020-1572.

Disclosure: The University of Miami and Dr. Gecheng Zha may receive royalties for future commercialization of the intellectual property used in this study.

References

[1] G. K. Batchelor. Axial flow in trailing line vortices. *Journal of Fluid Mechanics*, (20):645, 1964.

[2] C. E. Brown. Aerodynamics of Wake Vortices. *AIAA Journal*, 11(4):pp. 531–536, 1973.

[3] E. Anderson and T. Lawton. Correlation between Vortex Strength and Axial Velocity in a Trailing Vortex. *Journal of Aircraft*, 40(4):699, July 2003.

[4] T. Lee and J. Pereira. Nature of Wakelike and Jetlike Axial Tip Vortex Flows. *Journal of Aircraft*, 47(6), November 2010.

[5] K. W. McAlister and R. K. Takahashi. NACA 0015 Wing Pressure and Tailing Vortex Measurements. *NASA Technical Paper No. 3151*, 1991.

[6] M. O. Memon and A. Altman. Wingtip Vortex Behavior in the vicinity of the Maximum Lift to Drag Ration Lift Condition. In *54th AIAA Aerospace Sciences Meeting and Exhibit*, AIAA 2016-1847, San Diego, CA, January 2016.

[7] M. O. Memon, K. Wabick, A. Altman, and R. Buffo. Wing Tip Vortices from an Exergy-Based Perspective. *Journal of Aircraft, Special Section on Second High Lift Prediction Workshop*, 52:1267, 2015.

[8] Michael C. Rife Stergios I. Liapis Devenport, W.J. and Gordon J. Follin. The structure and dvelopment of a wing-tip vortex. *Journal of Fluid Mechanics*, (312):67.

[9] S. Gunasekaran and A. Altman. Is there a relationship between the turbulence character of free shear layer and the wingtip vortex? In *AIAA 2016-1068*, 54th Aerospace Sciences Meeting and Exhibit, San Diego CA, 2016.

[10] M. O. Memon and A. Altman. PIV Investigation into Cross-stream Behavior in Wing Wake Free Shear Layers: Challenges and Results. In *AIAA 2017-1461*, 55th AIAA Aerospace Sciences Meeting, Grapevine, TX, January 2017.

[11] G.-C. Zha and D. C. Paxton. A Novel Flow Control Method for Airfoil Performance Enhancement Using Co-Flow Jet. *Applications of Circulation Control Technologies*, Chapter 10, p. 293-314, Vol. 214, Progress in Astronautics and Aeronautics, AIAA Book Series, Editors: Joslin, R. D. and Jones, G.S., 2006.

[12] G.-C Zha and C. Paxton and A. Conley and A. Wells and B. Carroll. Effect of Injection Slot Size on High Performance Co-Flow Jet Airfoil. *AIAA Journal*, 43, 2006.

[13] G.-C. Zha and W. Gao and C. Paxton. Jet Effects on Co-Flow Jet Airfoil Performance. *AIAA Journal, No. 6*, 45:1222–1231, 2007.

[14] G.-C Zha and B. Carroll and C. Paxton and A. Conley and A. Wells. High Performance Airfoil with Co-Flow Jet Flow Control. *AIAA Journal*, 45, 2007.

[15] Wang, B.-Y. and Haddoukessouni, B. and Levy, J. and Zha, G.-C. Numerical Investigations of Injection Slot Size Effect on the Performance of Co-Flow Jet Airfoil . *AIAA Journal of Aircraft*, 45:2084–2091, 2008.

[16] B. P. E. Dano, D. Kirk, and G.-C. Zha. Experimental Investigation of Jet Mixing Mechanism of Co-Flow Jet Airfoil. AIAA Paper 2010-4421, 5th AIAA Flow Control Conference, Chicago, IL,, 28 Jun - 1 Jul 2010.

[17] B. P. E. Dano, G.-C. Zha, and M. Castillo. Experimental Study of Co-Flow Jet Airfoil Performance Enhancement Using Micro Discreet Jets. AIAA Paper 2011-0941, 49th AIAA Aerospace Sciences Meeting, Orlando, FL,, 4-7 January 2011.

[18] Lefebvre, A. and Dano, B. and Di Franzo, M. and Bartow, W. and Zha, G.-C. Performance of Co-Flow Jet Flow Airfoil with Variation of Mach Number. AIAA Paper 2013-0490, 51st AIAA Aerospace Science Meeting, Grapevine, TX, 7-10 Jan. 2013, to appear in Journal of Aircraft, 2016.

[19] Lefebvre, A. and Zha, G.-C. Numerical Simulation of Pitching Airfoil Performance Enhancement Using Co-Flow Jet Flow Control. AIAA Paper 2013-2517, 31st AIAA Applied Aerodynamics Conference, San Diego, CA, 24 - 27 June 2013.

[20] Lefebvre, A. and Zha, G.-C. . Design of High Wing Loading Compact Electric Airplane Utilizing Co-Flow Jet Flow Control. AIAA Paper 2015-0772, AIAA SciTech2015: 53nd Aerospace Sciences Meeting, Kissimmee, FL, 5-9 Jan 2015.

[21] Lefebvre, A. and Dano, B. and Bartow, W. and Di Franzo, M. and Zha, G.-C. Performance and Energy Expenditure of Co-Flow Jet Airfoil with Variation of Mach Number. *AIAA Journal of Aircraft*, 53:1757–1767, 2016.

[22] Liu, Z.-X. and Zha, G.-C. Transonic Airfoil Performance Enhancement Using Co-Flow Jet Active Flow Control. AIAA Paper 2016-3472, AIAA AVIATION 2016, 8th AIAA Flow Control Conference, Washington, D.C, June 13-17, 2016.

[23] Yang, Y.-C. and Zha, G.-C. Super-Lift Coefficient of Active Flow Control Airfoil: What Is the Limit? AIAA Paper 2017-1693, AIAA SCITECH2017, 55th AIAA Aerospace Science Meeting, Grapevine, Texas, 9-13 January 2017.

[24] G.-C. Zha, Y. Yang, Y. Ren, and B. McBreen. Super-Lift and Thrusting Airfoil of Coflow Jet Actuated by Micro-Compressors . AIAA Paper-2018-3061, AIAA AVIATION Forum 2018, 2018 Flow Control Conference, Atlanta, Georgia, June 25-29, 2018.

[25] P.R. Spalart and S.R. Allmaras. A One-equation Turbulence Model for Aerodynamic Flows. AIAA-92-0439, 1992.

[26] G.-C. Zha, Y. Shen, and B. Wang. An improved low diffusion E-CUSP upwind scheme . *Journal of Computer & Fluids*, 48:214–220, 2011.

[27] G.-C. Zha and E. Bilgen. Numerical Study of Three-Dimensional Transonic Flows Using Unfactored Upwind-Relaxation Sweeping Algorithm. *Journal of Computational Physics*, 125:425–433, 1996.

[28] B.-Y. Wang and G.-C. Zha. A General Sub-Domain Boundary Mapping Procedure For Structured Grid CFD Parallel Computation. *AIAA Journal of Aerospace Computing, Information, and Communication*, 5, No.11:2084–2091, 2008.

[29] Hu, Z.-J. PARALLEL COMPUTATION OF FLUID-STRUCTURAL INTERACTIONS USING HIGH RESOLUTION UPWIND SCHEMES. Ph.D. Thesis, University of Miami, Dept. of Mechanical and Aerospace Engineering, May 2005.

[30] Y.-Q. Shen J.-Y. Gan and G.-C Zha. Comparison of Drag Prediction Using RANS models and DDES for the DLR-F6 Configuration Using High Order Schemes. 54th Aerospace Sciences Meeting, San Diego, CA, AIAA Paper 2016-0553, 2016.

[31] Yang Wang and G.-C. Zha. Study of 3D Co-flow Jet Wing Induced Drag and Power Consumption at Cruise Conditions. San Diego, CA, 7-11 January 2019.

[32] Sidaard Gunasekaran. *Relationship between the Free Shear Layer, the Wingtip Vortex and Aerodynamic Efficiency*. Ph.d. thesis, University of Dayton, Dayton, Ohio, August 2016.

[33] Y. Wang and G.-C. Zha. "Study of Mach Number Effect for 2D Co-Flow Jet Airfoil at Cruise Conditions". AIAA Paper 2019-3169, AIAA Aviation 2019, AIAA Applied Aerodynamics Conference, Dallas, Texas, 17-21 June 2019.